Tailoring Catalytic Microenvironment of Cu_2O with SiO_2 to Enhance C_{2+} Products Selectivity in CO_2 Electroreduction

Tete Zhao[†], Jinhan Li[†], Jiuding Liu[†], Fangming Liu[†], Keqiang Xu[†], Meng Yu[†*], Wence Xu[†], and Fangyi Cheng[†‡*]

†Key Laboratory of Advanced Energy Materials Chemistry (Ministry of Education), Engineering Research Center of High-efficiency Energy Storage (Ministry of Education), College of Chemistry, Nankai University, Tianjin 300071, China;

‡Haihe Laboratory of Sustainable Chemical Transformations, Tianjin 300192, China.

[*]Corresponding author

Email: 819051@nankai.edu.cn; fycheng@nankai.edu.cn

1. MD simulations

To uncover the mechanism of enhanced C_{2+} products selectivity of CO_2RR by introducing the hydrophobic SiO_2 aerosol, coarse-grained molecular dynamic simulations (CGMD) were employed in this study. All the CGMD simulations were performed using GROMACS 4.6.7 software with Martini force field.[1,2] We aim to investigate the effect of Hydrophobic SiO_2 aerosol on the diffusion coefficients of H_2O and CO_2 both on Cu_2O and Cu_2O/SiO_2 electrodes. Before the simulations, we carefully constructed the Cu_2O by arranging several hydrophilic Nda-type (Nda is a parameter in the Martini force field, which represents hydrophilic) beads into a sheet with the shape of 8 nm in side length and 1.7 nm in height. The hydrophobic SiO_2 aerosol was constructed by arranging several hydrophobic C4-type (C4 is a parameter in the martini force field, which represents hydrophobic SiO_2) beads into a sphere with a diameter of 3 nm. The CO_2 bubbles were constructed by stacking 504 hydrophobic beads into a spherical shape with a diameter of 5 nm. The initial size of the simulation box was 8.0×8.0×16.0 nm^3 and full of water molecules. NVT ensemble (constant particle number, volume, and temperature) was used in our simulations. Temperature is kept as a constant at 300 K using the Berendsen weak coupling algorithm with a time constant of 1 ps. The neighbor list for nonbonded interactions was updated

every 10 steps. The Lennard-Jones potential was smoothly shifted to zero between 0.9 nm and 1.2 nm to reduce the cutoff noise. For electrostatic interactions, the coulombic potential, with a cutoff of 1.2 nm was smoothly shifted to zero from 0 to 1.2 nm. Herein, a time step of 20 fs was used for all simulations. Periodic boundary conditions were implemented in all three directions.

2. DFT calculations

Density functional theoretical (DFT) calculations were performed in Vienna Abinitio Simulation Package (VASP)[3] with plane wave basis sets and projector-augmented wave (PAW) pseudopotentials.[4] The generalized gradient approximation (GGA) developed by Perdew-Burke-Ernzerhof (PBE)[5] was implemented for exchange-correlation functions. The kinetic cutoff energy was set as 500 eV for the calculations. The structures were fully relaxed until the energy and the force on each atom converged 1×10^{-5} eV. The forces on the individual relaxed atoms was less than 0.02 eV/Å. The anion HCO_3^- was placed on the 2×2 Cu_2O (111) surface to simulate the energy change, in which HCO_3^- dissociates to form the protons and carbonates. The H_2O molecular was also placed on the 2×2 Cu_2O (111) surface to calculate the dissociation energy, which forms protons and hydroxyls. To avoid the interactions between periodic slabs, a vacuum space was inserted at the z direction at least 20 Å. A tow-layer (2×2) Cu_2O (111) surface was

constructed to calculate the dissociation of HCO_3^- and H_2O. Dipole corrections were included in all surface calculations in the surface normal direction (LDIPOL = TRUE, IDIPOL = 3). Over these optimized structures, vibration frequencies were calculated to obtain zero-point energies, thermal corrections, and entropy contributions, and the convergence tolerance was set to 1×10^{-6} eV. When calculating the vibration frequencies, only the adsorbed species were allowed to relax.

The dissociation process can be written as (an asterisk * represents the active site):

$$HCO_3 + * \rightarrow H_{ads} + CO_3^-{}_{ads} \qquad (s1\text{-}1)$$

$$H_2O + * \rightarrow H_{ads} + OH_{ads} \qquad (s1\text{-}2)$$

The Gibbs free energy change (ΔG) of each dissociation process was calculated by:

$$\Delta G = \Delta E + \Delta ZPE - T\Delta S \qquad (s1\text{-}3)$$

where ΔE, ΔZPE, T, and ΔS of each adsorbed state were obtained from DFT calculation, whereas the entropy for gas-phase molecules was taken from the NIST database. Here, the temperature T is 298.15 K.

3. Experimental section

3.1 Chemicals and reagents

SiO_2 (with a specific surface area of ~300 $m^2 g^{-1}$), ascorbic acid ($C_6H_8O_6$, A.R. grade), cupric chloride dihydrate ($CuCl_2 \cdot 2H_2O$, A.R. grade), sodium hydroxide (NaOH, purity≥ 98%), dimethyl sulfoxide (C_2H_6SO, G.C. grade) and isopropyl alcohol (C_3H_8O, A.R. grade) were purchased from Shanghai Aladdin Biochemical Technology Co., Ltd. Potassium bicarbonate ($KHCO_3$, purity ≥99.99% metals basis, 99.7-100.5% dry basis), absolute ethanol (C_2H_6O, Medicinal grade) were supplied by Shanghai Macklin Biochemical Co., Ltd. Deuterium oxide (D_2O, purity≥99.9%) was bought from Ai Lan (Shanghai) Chemical Technology Co., Ltd. Nafion D-521 dispersion, 5% W/W in water and 1-propanol, ≥0.92 meq/g exchange capacity was brought from the Alfa Aesar China Chemical Co., Ltd. Nafion 117 proton exchange membrane was bought from DuPont. All chemicals and reagents were purchased and used without further treatment.

3.2 Cu_2O synthesis

Cu_2O cubes were synthesized according to the previous report.[6] In short, a dilute solution of $CuCl_2$ was obtained by adding 7 mL 0.1 M $CuCl_2 \cdot 2H_2O$ to 300 mL of deionized water. Subsequently, 21 mL 0.2 M NaOH solution was added dropwise to the light blue solution for 10 minutes under continuous stirring. When the small light blue particles appeared, 14 mL 0.1 M $C_6H_8O_6$ solution was further added into the mixture solution drop by drop in less than 10 minutes.

The suspension was then stirred strictly for another hour after the color turned yellow. The Cu_2O cubes were precipitated by centrifugation and washed three times with deionized water and two times with absolute ethanol. Then the earthy yellow precipitation was transferred to a vacuum oven and dried at 60 ˚C overnight.

3.3 Preparation of Cu_2O and Cu_2O/SiO_2 electrodes

The Cu_2O slurry was prepared by ultrasonically blending 10 mg Cu_2O, 1 mL of isopropyl alcohol, and 20 μL of 5% Nafion solution for 30 minutes until forming the uniform suspension. Subsequently, 20 μL of the obtained Cu_2O slurry was carefully dropped on the surface of carbon glassy (diameter, 6mm) and thoroughly dried at room temperature. This working electrode was named Cu_2O and the loading was 0.708 mg cm^{-2}. To prepare the Cu_2O/SiO_2 working electrode, different dosages of hydrophobic SiO_2 aerosol were first dissolved into 1 mL of isopropyl alcohol and sonicated to form clear suspension. Secondly, different concentrations of suspensions of hydrophobic SiO_2 aerosol and the 10 mg mL^{-1} of Cu_2O were instantly blended by sonication. The Cu_2O/SiO_2-x (x represents the concentration of hydrophobic SiO_2 aerosol, and corresponds to 1, 2, 3, 4, and 5 mg mL^{-1}) compound slurry was obtained for further use. For example, Cu_2O/SiO_2-2 electrode was prepared by mixing the hydrophobic SiO_2 solution with 2

mg mL^{-1} and Cu_2O suspension with 10 mg mL^{-1}. For short, the Cu_2O/SiO_2-2 working electrode was abbreviated as Cu_2O/SiO_2. The Cu_2O/SiO_2-1, Cu_2O/SiO_2-3, Cu_2O/SiO_2-4, and Cu_2O/SiO_2-5 working electrodes were prepared followed by the Cu_2O/SiO_2-2 electrode. Then, we prepared the hydrophobic working electrode Cu_2O/SiO_2 by dropped the 40 μL as-prepared suspension onto the carbon glassy and dried at room temperature. The loading of Cu_2O/SiO_2 working electrode was the same as the Cu_2O working electrode.

3.4 In situ infrared spectroscopy investigations

Electrochemical in situ FT-IR reflection spectroscopy was investigated on a Fourier transform infrared spectrometer (FTIR, Nicolet iS50, Thermo Fisher Scientific, USA) equipped with Mercury Cadmium Tellurid (MCT) detector, which was cooled with the liquid nitrogen atmosphere for protection and drove the interferential CO_2 in the atmosphere. We adopted the three electrodes test system to evaluate the change at the surface of the Cu_2O and Cu_2O/SiO_2 working electrodes. The reflective window was made up of CaF_2 crystal. The working electrodes were prepared by supporting the catalyst ink on the surface of carbon glassy (diameter 5 mm) and dried at room temperature before measurements. Real-time FTIR spectra were recorded during the chronopotentiometry test. The working potentials from open circuit potential (OCP) to

−1.2 V vs. RHE in a CO_2-saturated 0.1 M $KHCO_3$. The stepping width and test time are 100 mV and 80 s, respectively.

3.5 Electrochemical CO_2 reduction and gaseous product analysis

The electrochemical measurements were implemented using an electrochemistry workstation (CHI760e, CH, Shanghai). We adopted the self-designed gas-tight H-type electrochemical cell separated by a proton exchange membrane (Nafion N-117, Dupont, USA) to evaluate the electrochemical performance of the Cu_2O and Cu_2O/SiO_2 working electrodes. The electrolyte solution was prepared by dissolving the specific dosage of potassium bicarbonate in Milli-Q water to form the uniform 0.1 M $KHCO_3$ solution. The three-electrode compartment was adopted to evaluate the performances of different working electrodes. Working electrodes were prepared by as-prepared Cu_2O dropped onto the surface of glassy carbon. A Pt foil was used as the counter electrode and an Ag/AgCl electrode (saturated KCl) as a reference electrode. All potentials were converted to scales against an RHE reference: E (vs. RHE) = E (vs. Ag/AgCl) + 0.0592 pH + 0.198 V. All the potentials are iR-compensated by 85%. The potentials were compensated as E (iR corrected vs. RHE) = E (vs. RHE) - Rs×I. Rs is the 0.1 M $KHCO_3$ solution resistance, which was measured by EIS performing on a CHI760e electrochemistry workstation at a frequency

range of 10^{-2}~10^{5} and fitted by Z-plot software. The cathodic compartment was added to 35 mL 0.1 M $KHCO_3$ solution and the anodic compartment was added to 30 mL 0.1 M $KHCO_3$ solution to maintain the balance of the level of liquid to avoid the difference in dropout voltage. Before testing, the 0.1 M $KHCO_3$ solution in the cathodic compartment was saturated by bubbling CO_2 gas for 30 minutes until the 0.1 M $KHCO_3$ solution was saturated (pH = 6.8). In a typical electrolysis process, the reactions were maintained for a specific time with continuous CO_2 bubbling at a flow rate of 6.8 mL min^{-1}. In real-time electrolysis, the gaseous products were directly purged into the gas chromatograph (GC, Shimadzu 2010 plus) equipped with the BID detector to analyze the generated H_2, CO, CH_4, and C_2H_4. Ultrapure helium (＞99.9999%) was used as carrier gas.[7,8]

3.6 Liquid products identification and quantification

After each electrolysis at different potentials, 30 mL electrolyte was taken out from the H-type electrochemical cell for further analysis. Then, 20 μL DMSO as the internal standard was added into the 30 mL electrolyte solution. Afterwards, 450 μL mixed electrolyte and 50 μL D_2O were transferred to a nuclear magnetic resonance (NMR) sample tube and analyzed by ^1H NMR spectroscopy using the 400 MHz spectrometers (Quantum-1, Zhongke-Niujin MR Tech Co.Ltd,

China) and identifying the liquid products in an electrolyte. The signal of water was suppressed. The ^{1}H peak area of each product in the electrolyte was calculated by the ^{1}H peak area of the confirmed concentration of DMSO to quantity the concentration of products.[9,10]

4. Material characterization

Morphologies and microstructures of as-prepared Cu_2O were performed on a Field emission scanning electron microscopy (SEM, JSM-7900F, JEOL, Japan) at an accelerating voltage of 1.0 kV and high-resolution transmission electron microscopy (HRTEM, Talos F200X G2, FEI Czech Republic, Czech Republic) equipped with EDS. Surface compositions and chemical valence of the catalysts were characterized with X-ray photoelectron spectroscopy (XPS, PHI5000VersaProbe, Ulvac-phi, Japan) with an Al Kα X-ray source at a power of 44.9 W. High-resolution spectra of Cu 2p and Cu auger LMM were recorded with a 23.5 eV pass energy and 187.85 eV for the XPS survey. The XPS spectra were aligned to the binding energy of C 1s at 284.8 eV for all samples and fitted by XPSPEAK41 software. Ex-situ Fourier transforms infrared spectra were recorded on a Nicolet iS50 infrared spectrometer (Thermo Fisher Scientific, USA) equipped with Mercury Cadmium Telluride (MCT) detector and KBr beam splitter. The crystal structures of the samples were analyzed by X-ray diffraction (XRD,

MimFLex600, Rigaku, Japan) spectroscopy with Cu Kα radiation (40 kV, λ=1.5406 Å and 15 mA) at a scan rate of 8° min^{-1} with 2 theta degree range from 5° to 85°. Nitrogen adsorption-desorption measurements and surface area were studied on a Micromeritics ASAP 2460 analyzer (USA). Pore volumes and pore sizes were calculated using the density functional theory (DFT) methods according to the pore-size distribution curves from the desorption isotherms. The carbon dioxide adsorption-desorption curves were performed on surface area and microporous analyzer (BSD-PM, Beishied instrument technology, China) at 298.15 K. The contact angles were obtained on dataphysics (OCA25, dataphysics, Germany) with 10 μL electrolyte dropped onto the surface of the working electrodes, hydrophobic SiO_2 aerosol, and the glassy carbon electrode.

5. Additional results and discussion

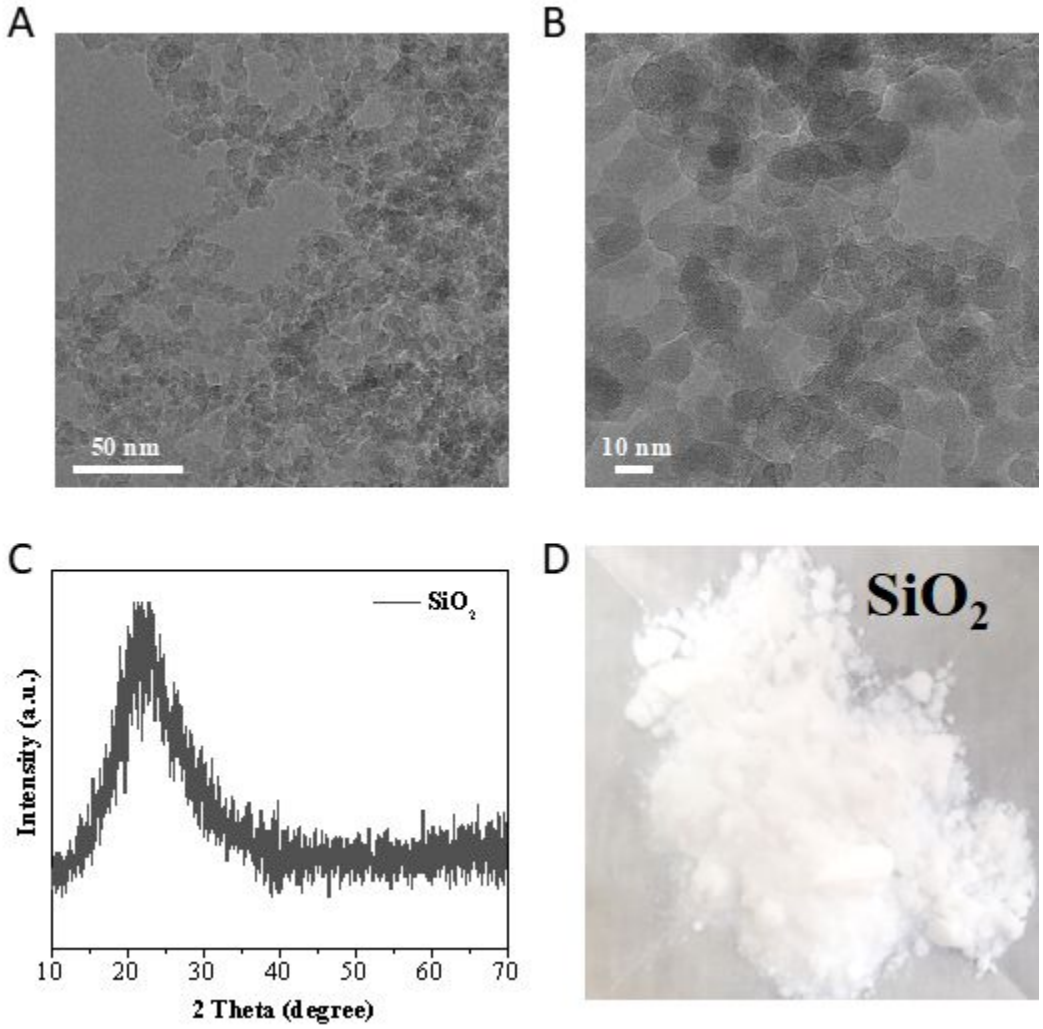

Figure S1. (A, B) TEM and HRTEM images, (C) XRD pattern and (D) digital photograph of amorphous SiO_2.

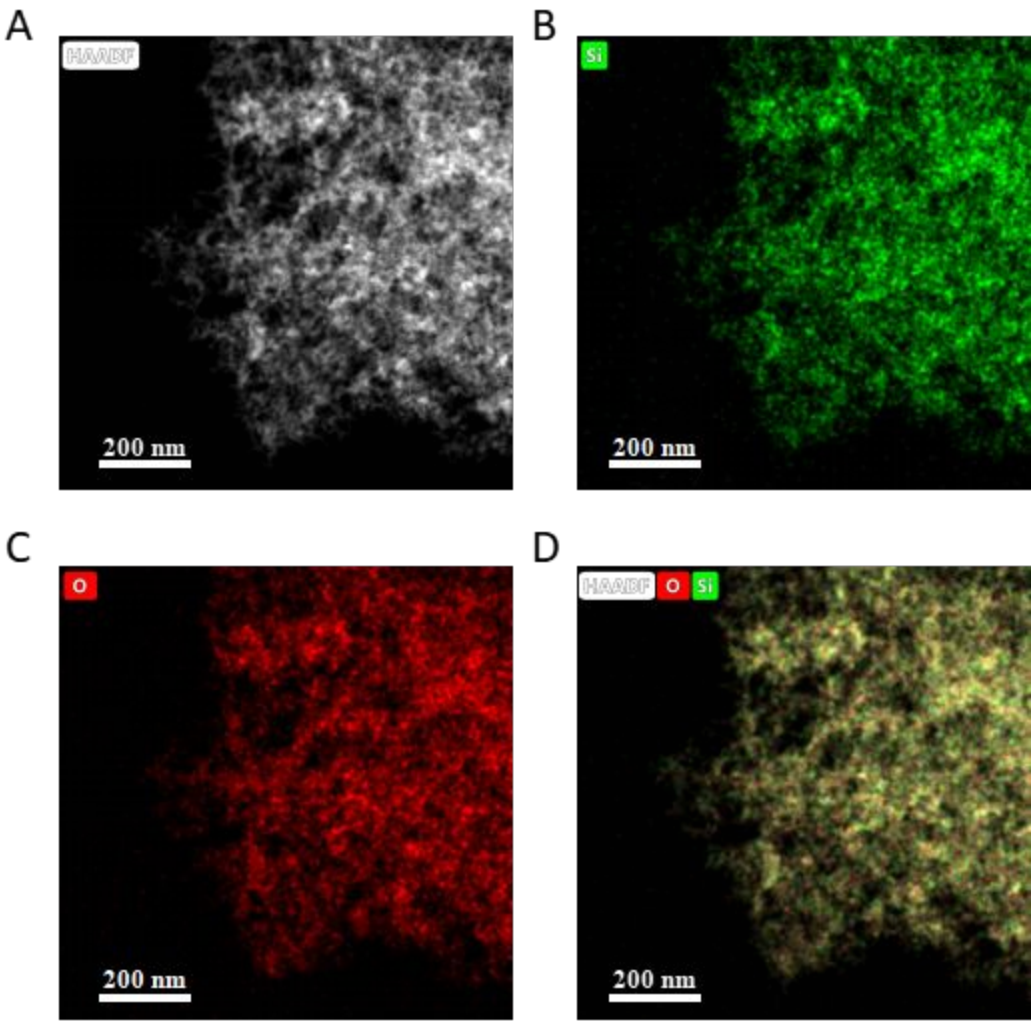

Figure S2. (A) HADDF-STEM and corresponding elemental mapping images of (B) Si (green) and (C) O (red) and (D) the elements mixed of amorphous SiO_2.

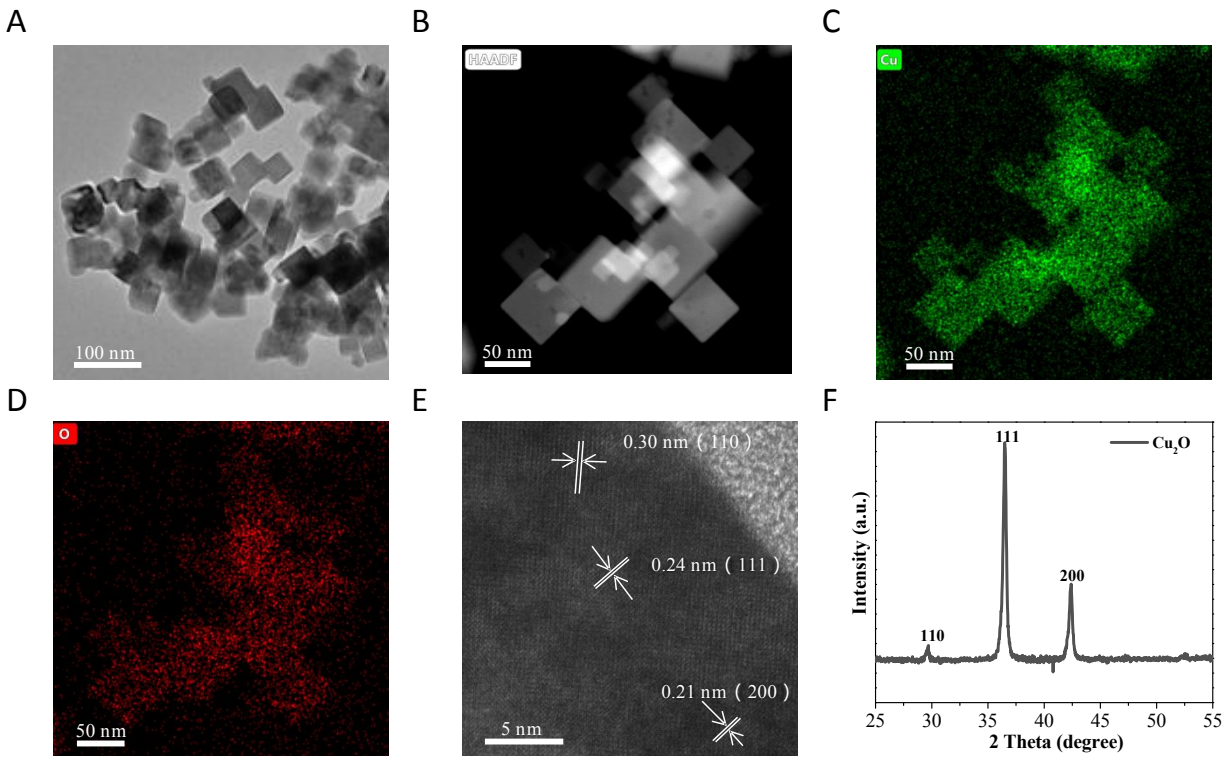

Figure S3. (A) TEM and (B) HAADF-STEM and corresponding elemental mapping images with (C) Cu (green), (D) O (red), (E) HRTEM images and (F) XRD pattern of Cu_2O.

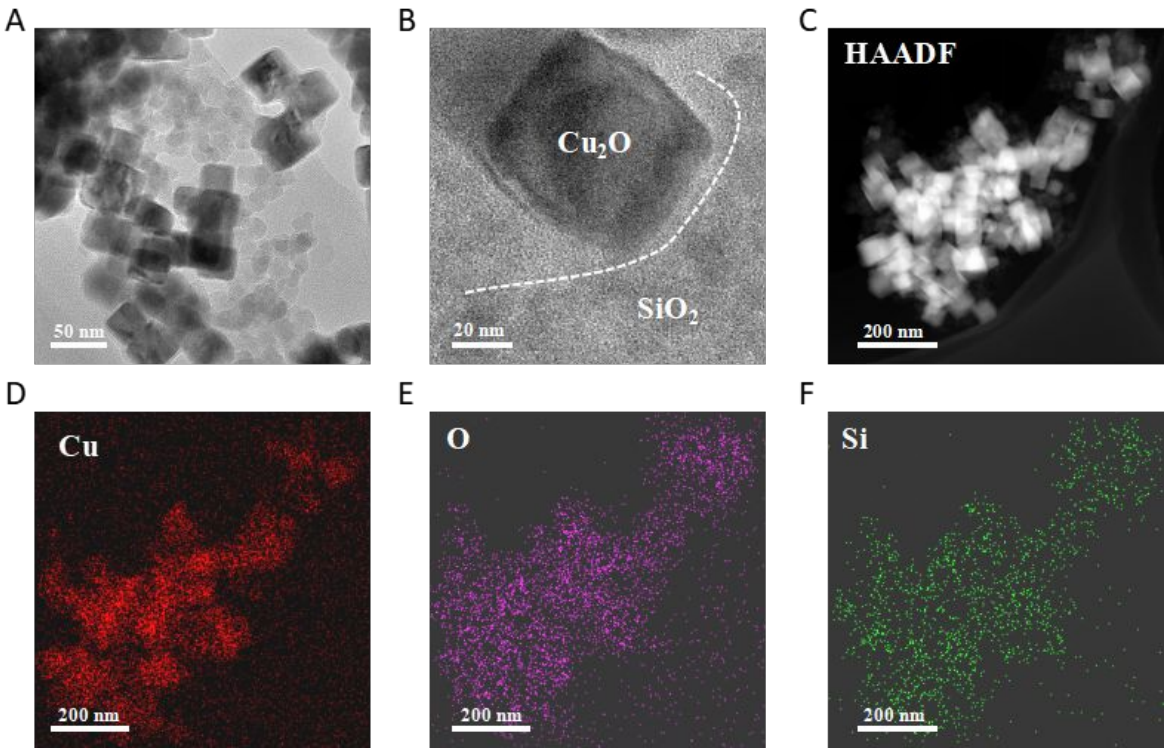

Figure S4. (A) TEM, (B) HRTEM, (C) HADDF-STEM images of Cu_2O/SiO_2 composites, the corresponding elemental mapping images with (D) Cu (red), (E) O (purple), (F) Si (green).

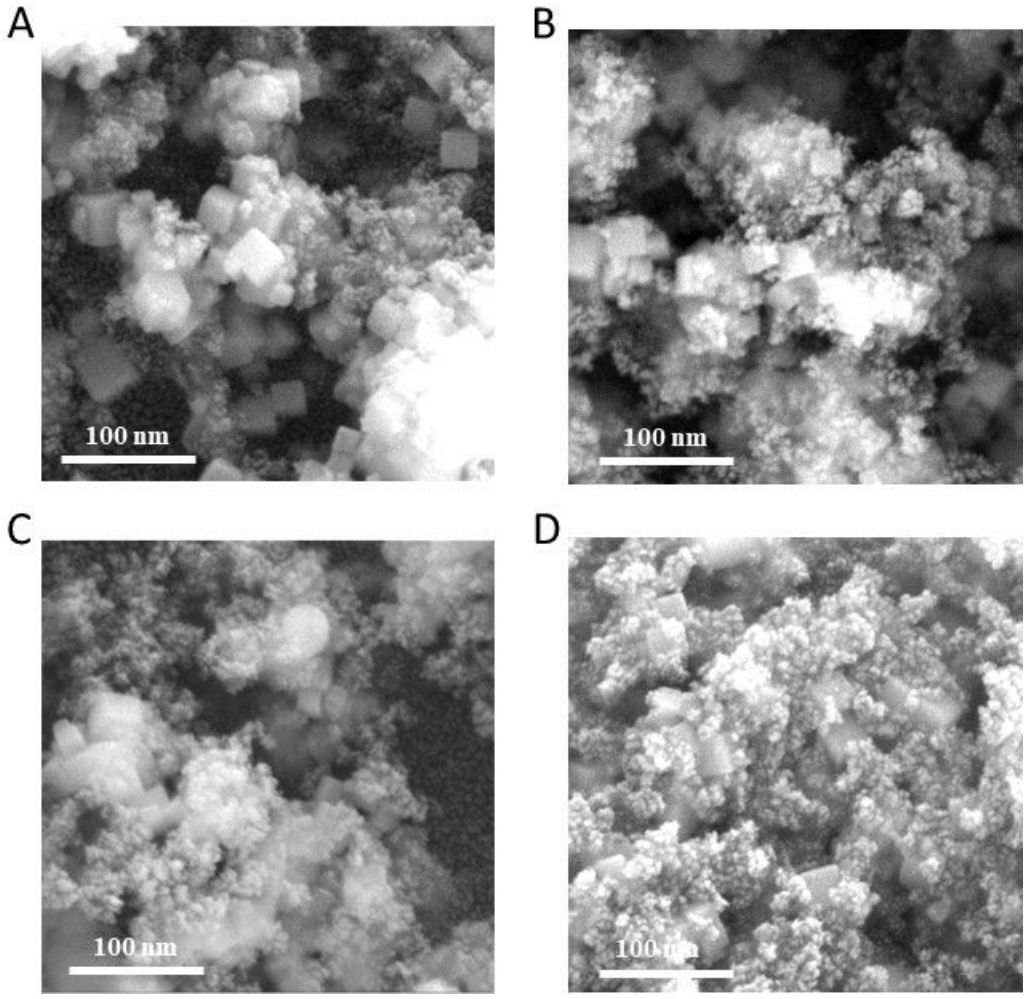

Figure S5. SEM images of (A) Cu_2O/SiO_2-1, (B) Cu_2O/SiO_2-3, (C) Cu_2O/SiO_2-4 and (D) Cu_2O/SiO_2-5.

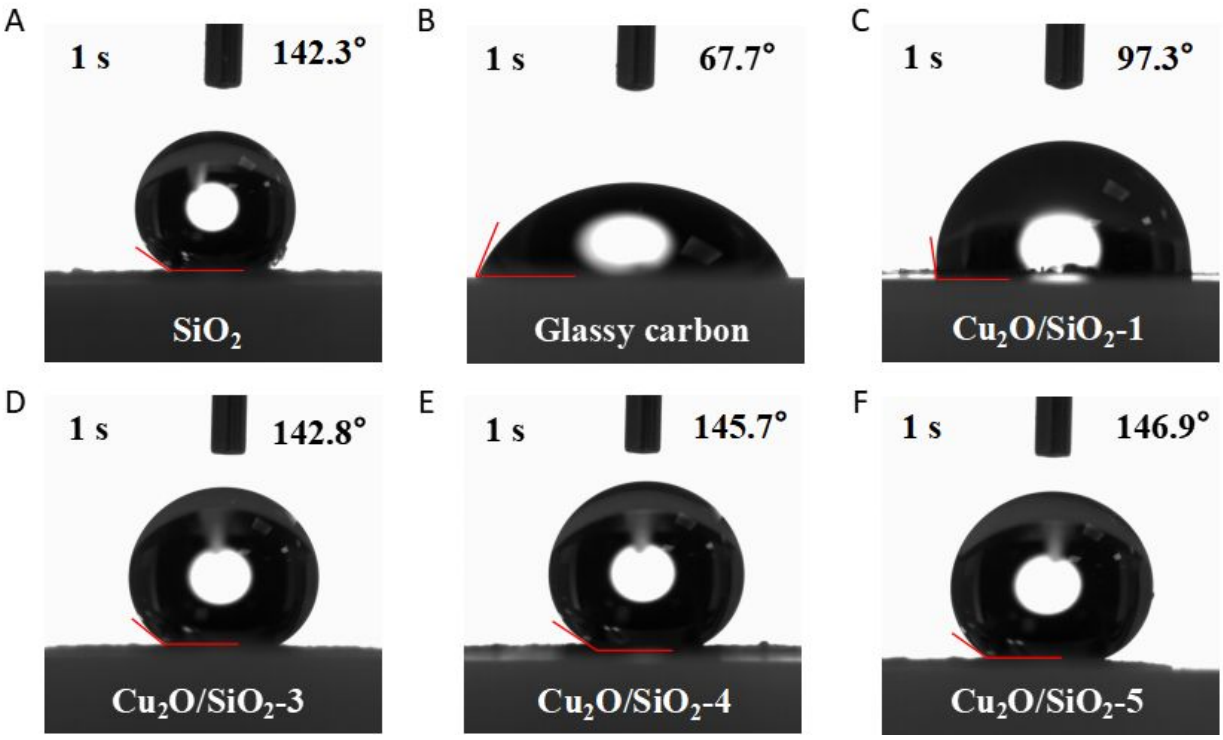

Figure S6. Contact angle of (A) SiO_2, (B) glassy carbon, (C) Cu_2O/SiO_2-1, (D) Cu_2O/SiO_2-3, (E) Cu_2O/SiO_2-4 and (F) Cu_2O/SiO_2-5.

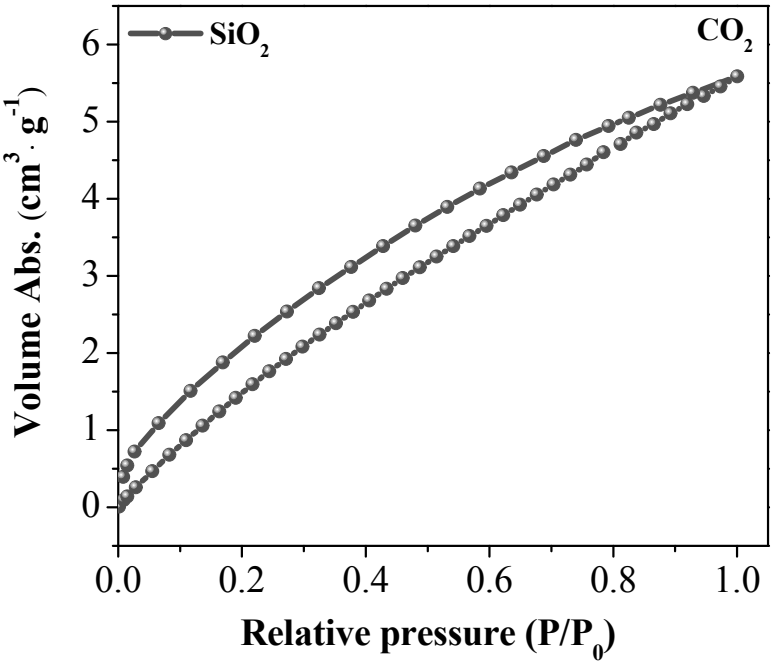

Figure S7. CO_2 adsorption-desorption curves of SiO_2.

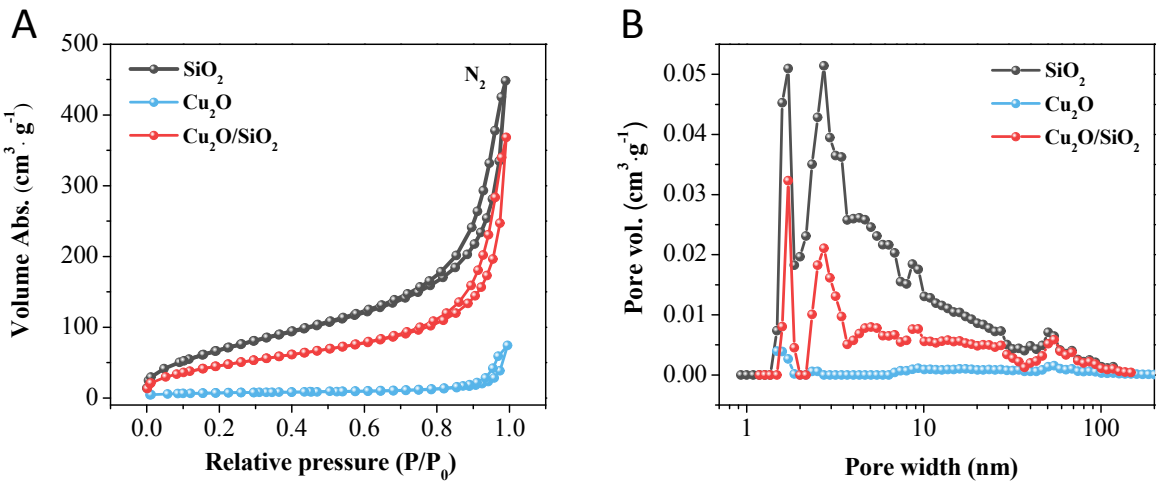

Figure S8. (A) N_2 adsorption-desorption curves of Cu_2O, Cu_2O/SiO_2, and SiO_2 and (B) corresponding pore diameter distribution curves.

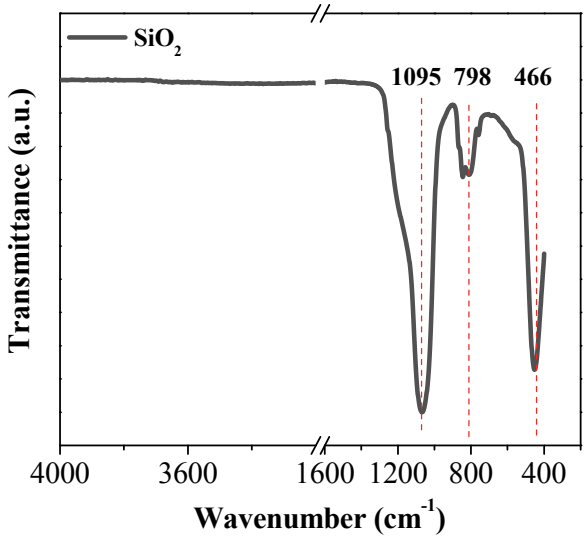

Figure S9. FTIR spectrum of SiO_2.

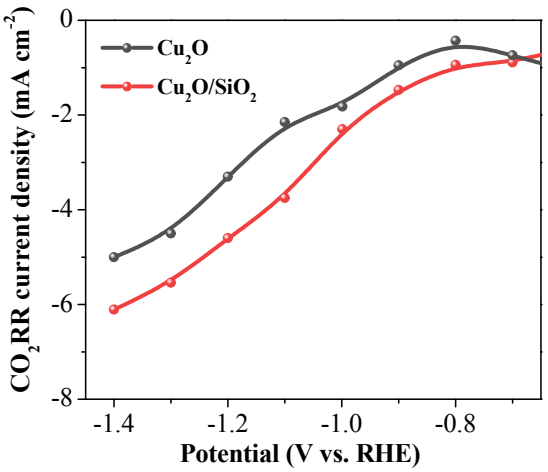

Figure S10. Partial current densities for CO_2RR on the Cu_2O and Cu_2O/SiO_2 electrodes at various potentials with CO_2-saturated 0.1M $KHCO_3$.

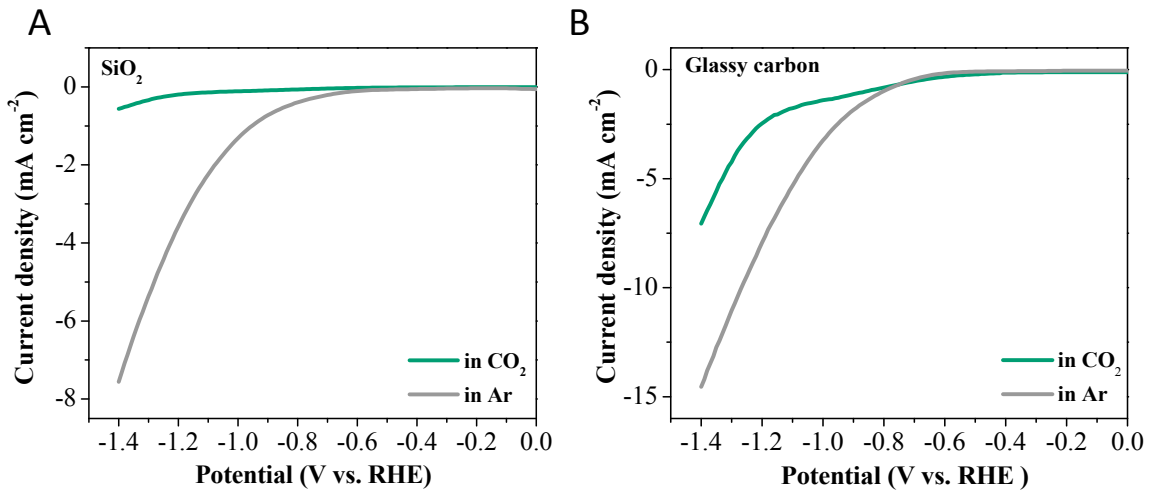

Figure S11. LSV curves of (A) SiO_2 and (B) glassy carbon in CO_2/Ar-saturated 0.1 M $KHCO_3$.

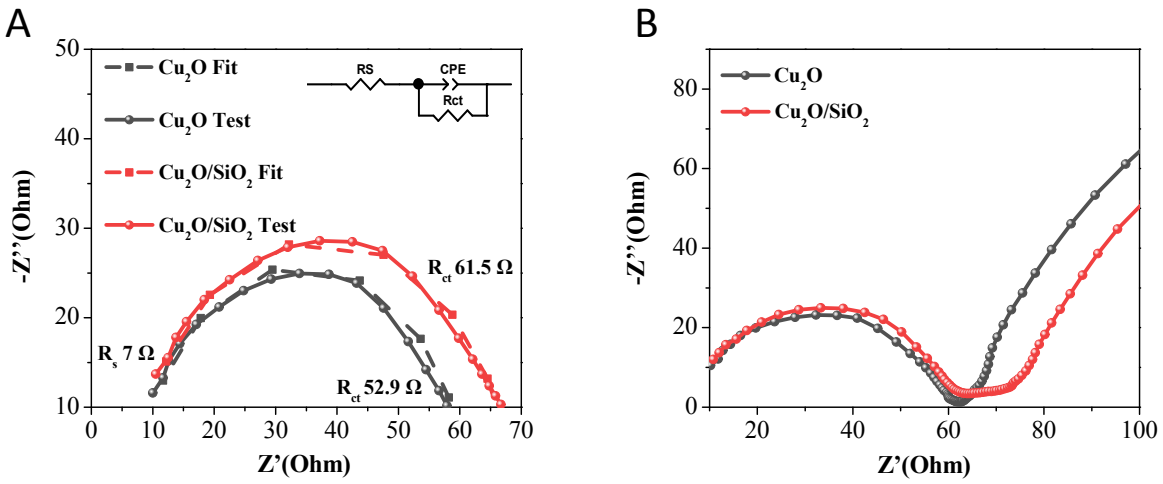

Figure S12. (A) Nyquist plots obtained at the specific potential in CO_2-saturated 0.1 M $KHCO_3$ and the corresponding fitting equivalent circuit diagram on Cu_2O and Cu_2O/SiO_2, (B) EIS spectra of Cu_2O and Cu_2O/SiO_2 from the 100 kHz to 0.01 Hz.

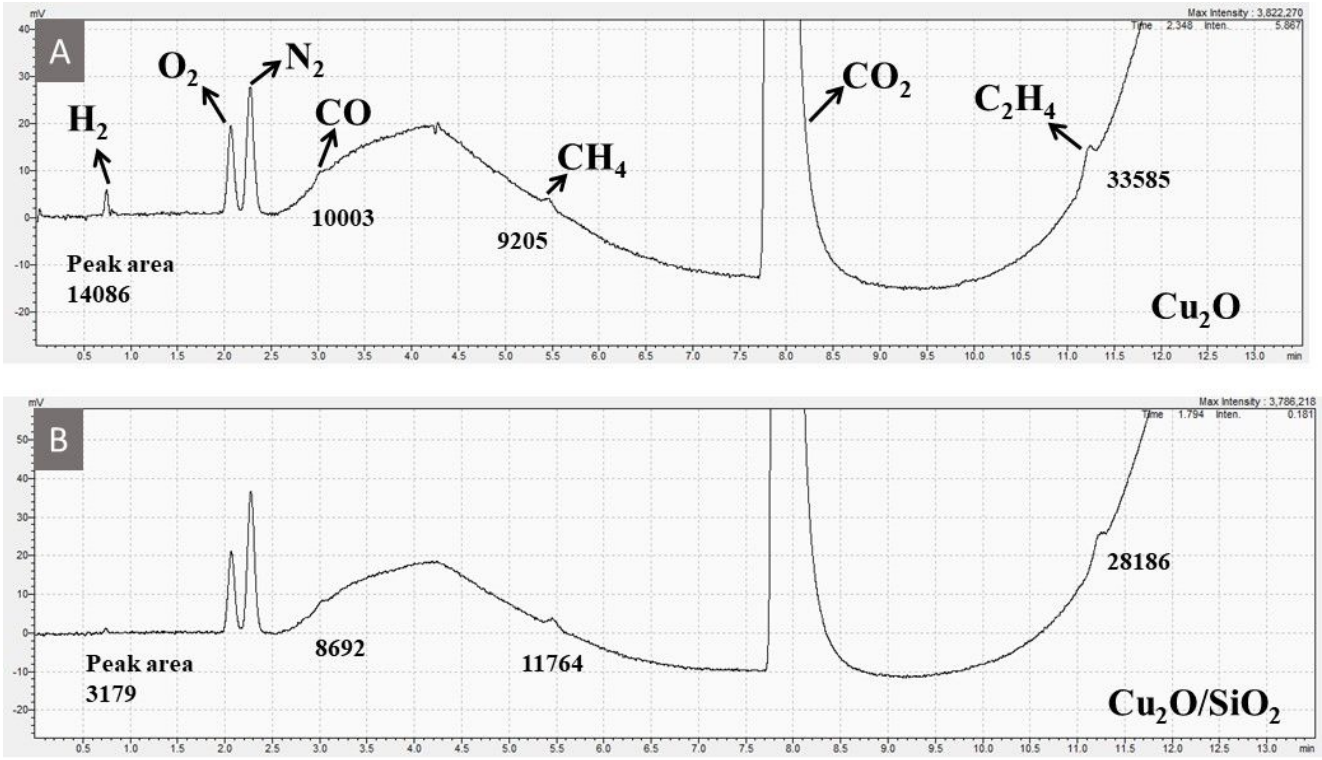

Figure S13. Gas chromatography (GC) data recorded after electrolysis on (A) Cu_2O, and (B) Cu_2O/SiO_2 at −1.2 V vs. RHE.

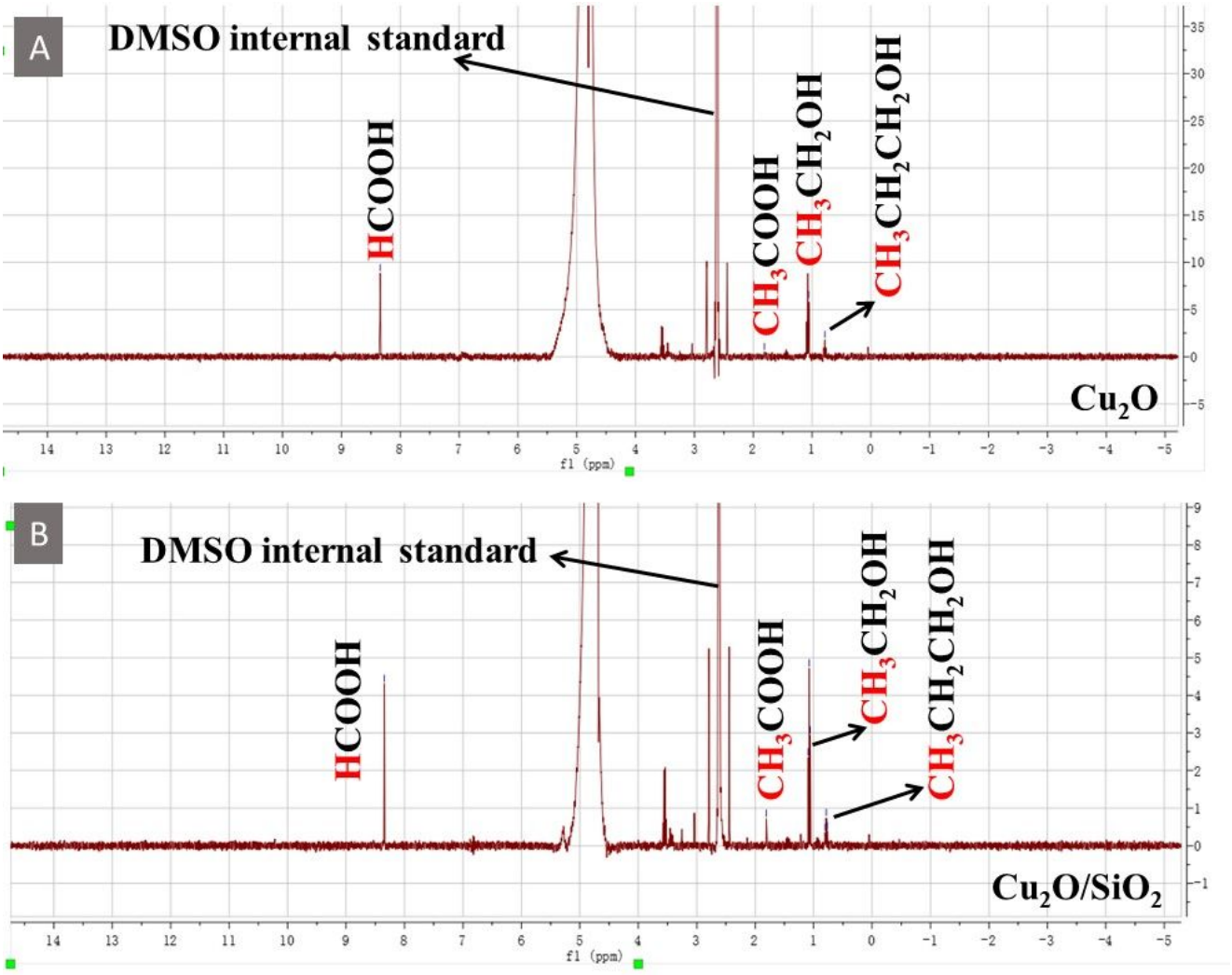

Figure S14. Spectra of ^{1}H NMR record after the CO_2RR on (A) Cu_2O, and (B) Cu_2O/SiO_2 at −1.2 V vs. RHE.

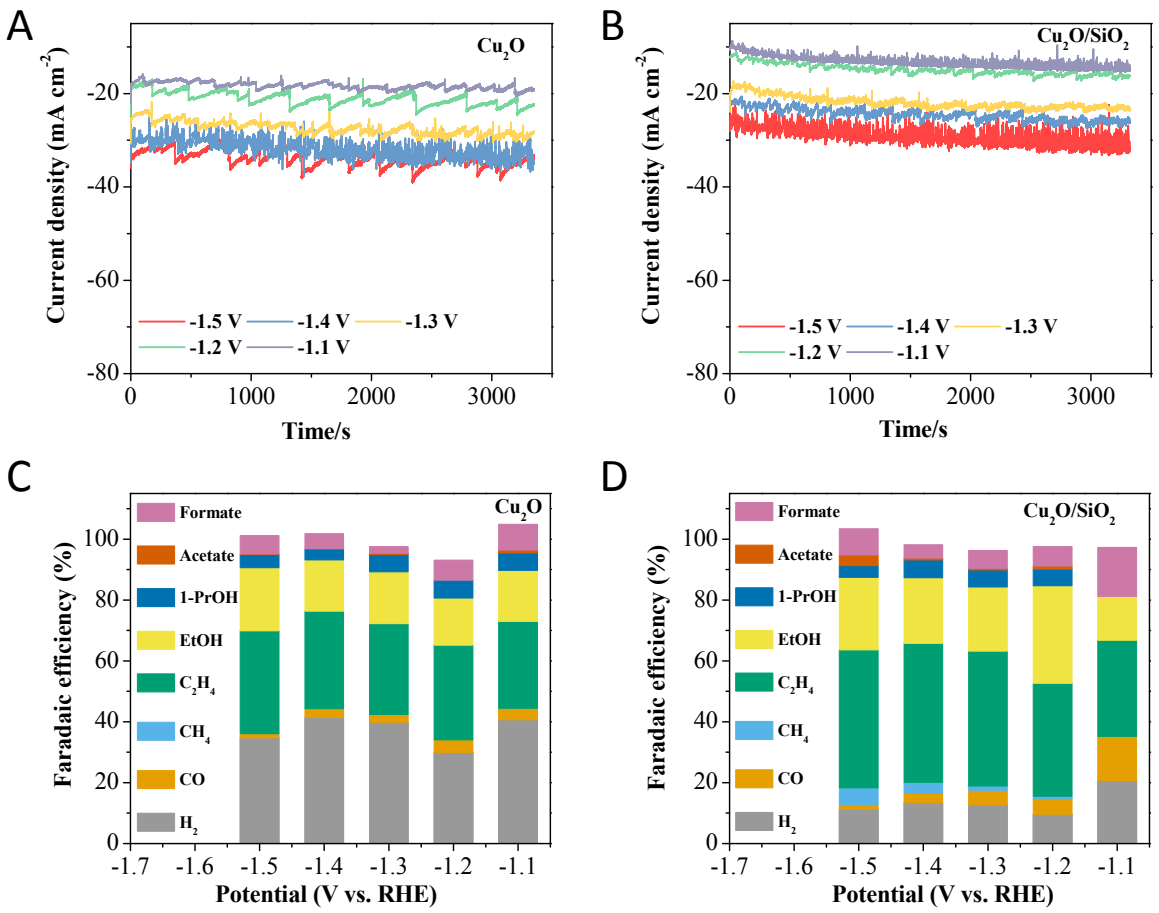

Figure S15. (A, B) The i-t curves recorded in CO_2-saturated 0.1 M $KHCO_3$ at various potentials for Cu_2O (A), and Cu_2O/SiO_2 (B) in the H-type cell. (C, D) The corresponding Faradaic efficiency for Cu_2O (C) and Cu_2O/SiO_2 (D).

Table S1. The FE of H_2 and C_{2+} products using various copper-based catalysts for CO_2RR in the reported literature.

Catalysts	Substrates	Cell type	Electrolyte	E (vs. RHE)	Faradaic efficiency (FE, %)		Ref
					H_2	C_{2+}	
Cu_2O/SiO_2	Glassy carbon	H-cell	0.1 M $KHCO_3$	−1.20 V	9.6	75.6	This work
Cu_2O	Carbon paper		0.1 M $KHCO_3$	−1.05 V	18.0	60	11
Nano wrinkled Cu	Glassy carbon		0.1 M $KHCO_3$	−1.10 V	-	57	12
Cu	-		0.1 M $KHCO_3$	−1.00 V	＜10%	76	13
Cu_2O NP/C	Glassy carbon		0.1 M $KHCO_3$	−1.20 V	30	73	14
Polycrystalline Copper	Cu disk		0.1 M $KHCO_3$	−1.10 V	15.5	78.2	15
Cu nano cube	Glassy carbon		0.1 M $KHCO_3$	−1.00 V	-	73	16
Cu_4Zn	Glassy carbon		0.5 M $KHCO_3$	−1.05 V	42.28	51.38	17
CuAg alloy	Carbon paper	Flow cell	1 M KOH	−0.70 V	9.8	85.1	18
Cu-CuI	Carbon paper		1 M KOH	−0.87 V	10-15	71	19
$CuO-CeO_2$	PTFE membrane		1 M KOH	−1.12 V	-	78.2	20
Hierarchical Copper	Cu GDE		1 M KOH	−0.68 V	17.54	63	21
Cu nanoparticles	Carbon paper		1 M KOH	−0.87 V	7	70	22

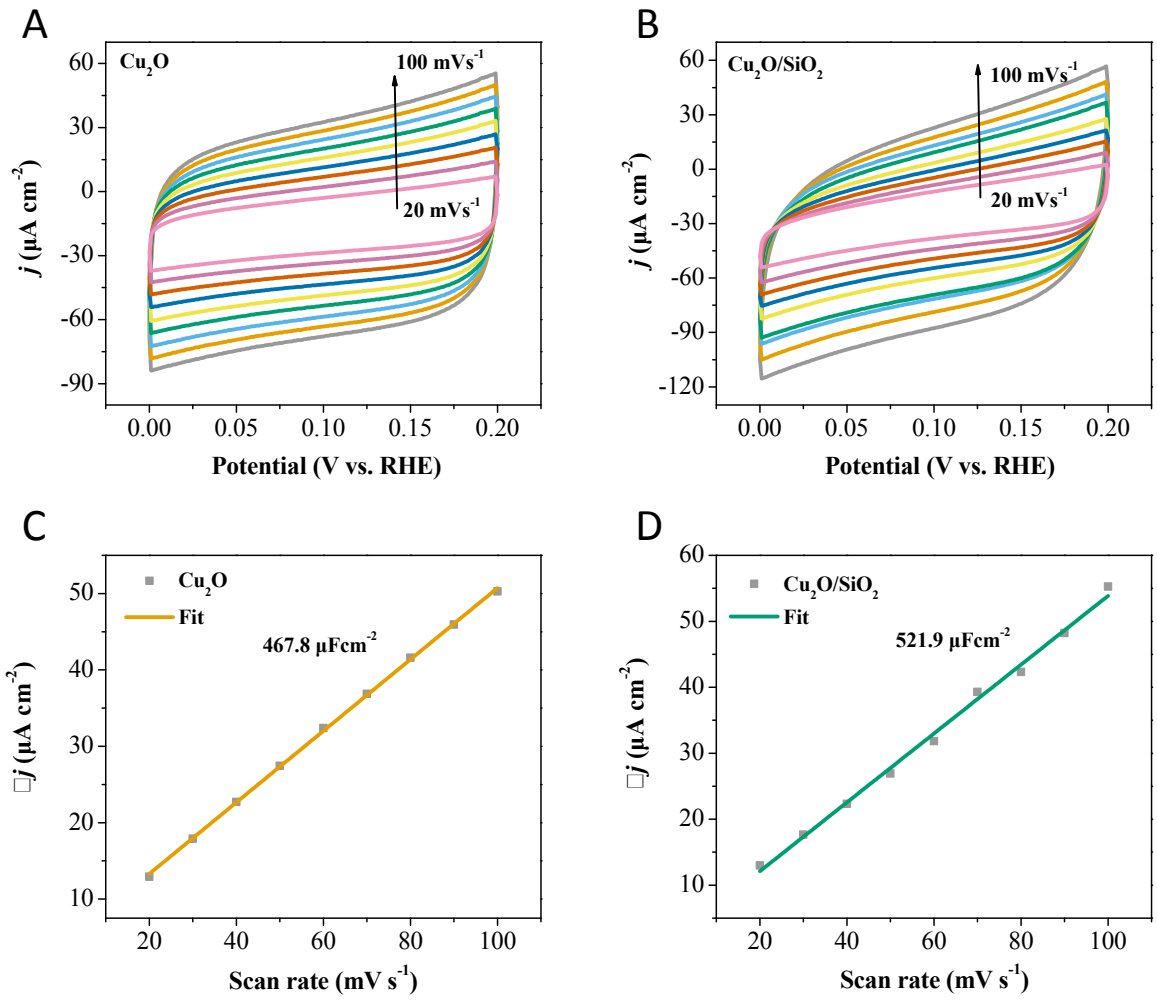

Figure S16. (A, B) Cyclic voltammograms of Cu_2O (A) and Cu_2O/SiO_2 (B) in Ar-saturated 0.1 M $KHCO_3$ scanned from 0.0 to 0.2 V vs. RHE at different scan rates. (C, D) Current density plotted against CV scan rates for (C) Cu_2O and (D) Cu_2O/SiO_2.

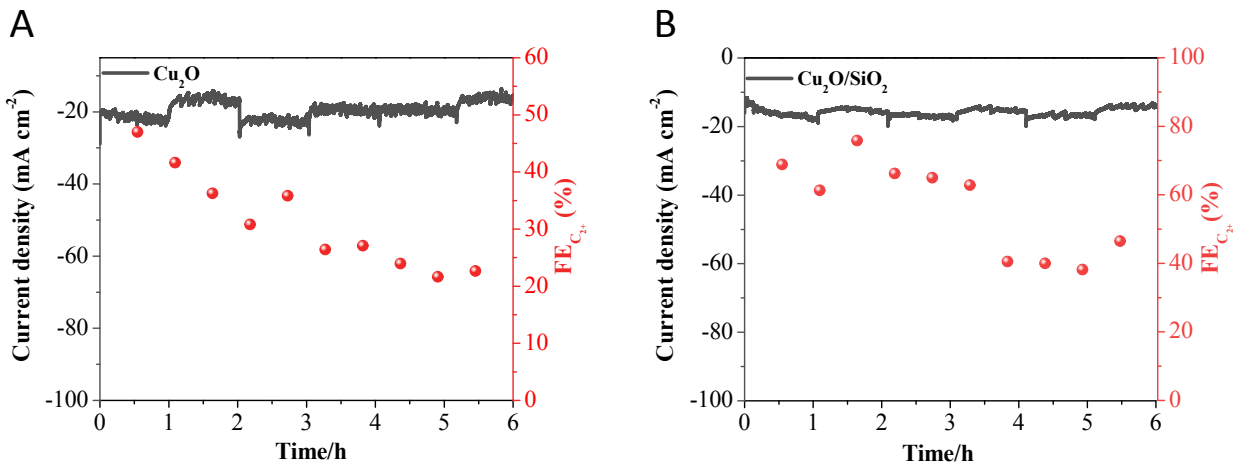

Figure S17. Stability tests were performed on Cu_2O (A) and Cu_2O/SiO_2 (B) electrodes for 6 h at −1.2 V vs. RHE in CO_2-saturated 0.1 M $KHCO_3$. The right axis is the corresponding Faradaic efficiency of C_{2+} products.

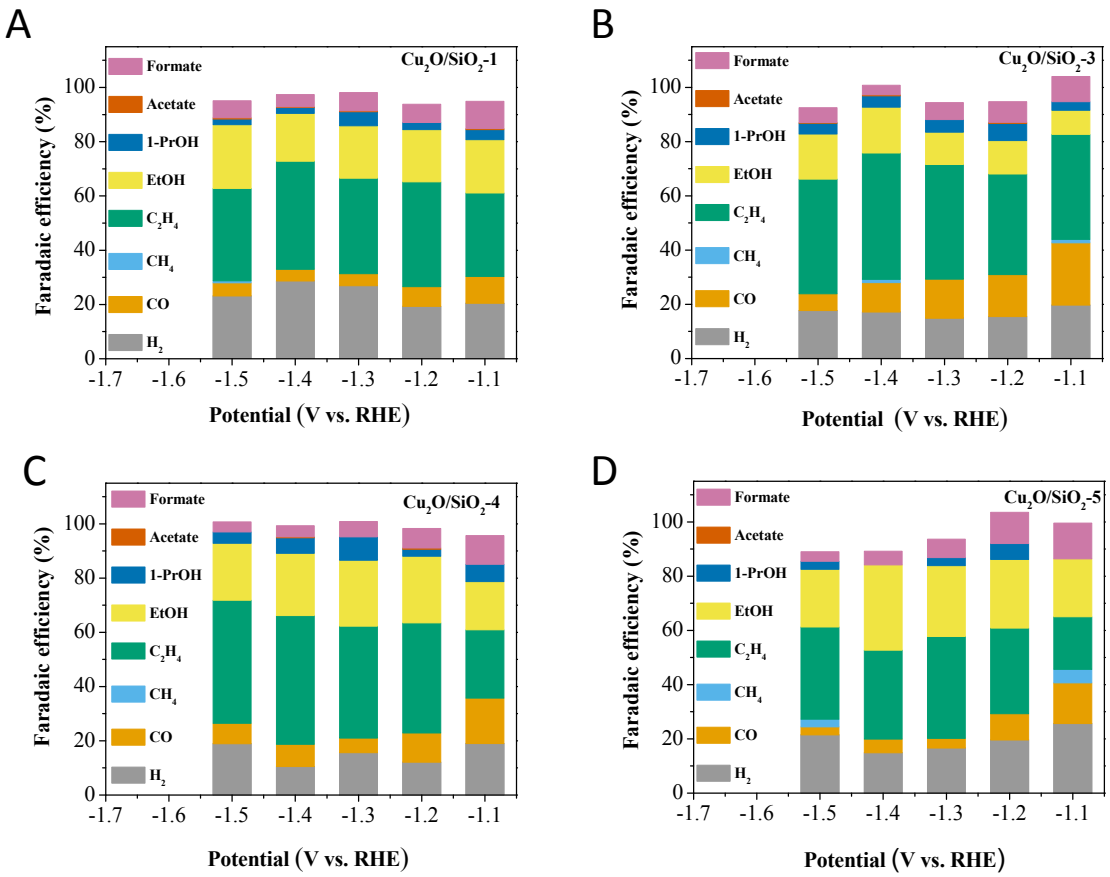

Figure S18. The products distribution of (A) Cu_2O/SiO_2-1, (B) Cu_2O/SiO_2-3, (C) Cu_2O/SiO_2-4 and (D) Cu_2O/SiO_2-5.

Table S2. Faradaic efficiencies of CO_2 electroreduction products on Cu_2O/SiO_2-1/3/4/5 composites electrodes under different applied potentials.

Catalysts (Potential vs. RHE)	Faradaic efficiency (%)								
	H_2	CO	CH_4	C_2H_4	C_2H_5OH	C_3H_7OH	CH_3COOH	HCOOH	Total
Cu_2O/SiO_2-1 (−1.1 V)	20.44	9.91	0	30.78	19.61	3.71	0.4	10.02	94.87
Cu_2O/SiO_2-1 (−1.2 V)	19.29	7.28	0	38.65	19.24	2.62	0	6.71	93.79
Cu_2O/SiO_2-1 (−1.3 V)	26.89	4.49	0	35.2	19.3	5.16	0.33	6.77	98.14
Cu_2O/SiO_2-1 (−1.4 V)	28.66	4.33	0	39.83	17.64	2.15	0.23	4.54	97.38
Cu_2O/SiO_2-1 (−1.5 V)	23.17	4.84	0.75	34.00	23.50	2.10	0.46	6.27	95.09
Cu_2O/SiO_2-3 (−1.1 V)	19.76	22.90	1.32	38.69	8.89	3.18	0	9.27	104.01
Cu_2O/SiO_2-3 (−1.2 V)	15.47	15.47	0	37.13	12.31	6.32	0.44	7.59	94.73
Cu_2O/SiO_2-3 (−1.3 V)	14.86	14.43	0	42.31	11.90	4.64	0	6.29	94.43
Cu_2O/SiO_2-3 (−1.4 V)	17.17	10.82	1.21	46.59	16.90	4.17	0.44	3.51	100.81
Cu_2O/SiO_2-3 (−1.5 V)	17.73	6.14	0	42.30	16.67	3.95	0.25	5.44	92.48
Cu_2O/SiO_2-4 (−1.1 V)	19.00	16.74	0	25.18	17.77	6.44	0	10.52	95.65
Cu_2O/SiO_2-4 (−1.2 V)	12.13	10.76	0	40.58	24.63	2.52	0.46	7.21	98.29
Cu_2O/SiO_2-4 (−1.3 V)	15.65	5.36	0	41.28	24.31	8.59	0	5.70	98.19
Cu_2O/SiO_2-4 (−1.4 V)	10.50	8.19	0	47.48	22.97	5.72	0.34	4.11	99.31

Cu_2O/SiO_2-4 (−1.5 V)	18.95	7.51	0	45.41	20.97	4.18	0	3.72	100.74
Cu_2O/SiO_2-5 (−1.1 V)	25.62	15.03	5.00	19.40	21.34	0	0	13.18	99.57
Cu_2O/SiO_2-5 (−1.2 V)	19.58	9.70	0	31.57	25.30	5.90	0	11.52	103.57
Cu_2O/SiO_2-5 (−1.3 V)	16.61	3.59	0	37.6	26.06	3.01	0	6.78	93.65
Cu_2O/SiO_2-5 (−1.4 V)	14.87	5.03	0	32.83	31.44	0	0	5.06	89.23
Cu_2O/SiO_2-5 (−1.5 V)	21.50	2.92	2.87	34.00	21.29	2.95	0	3.51	89.04

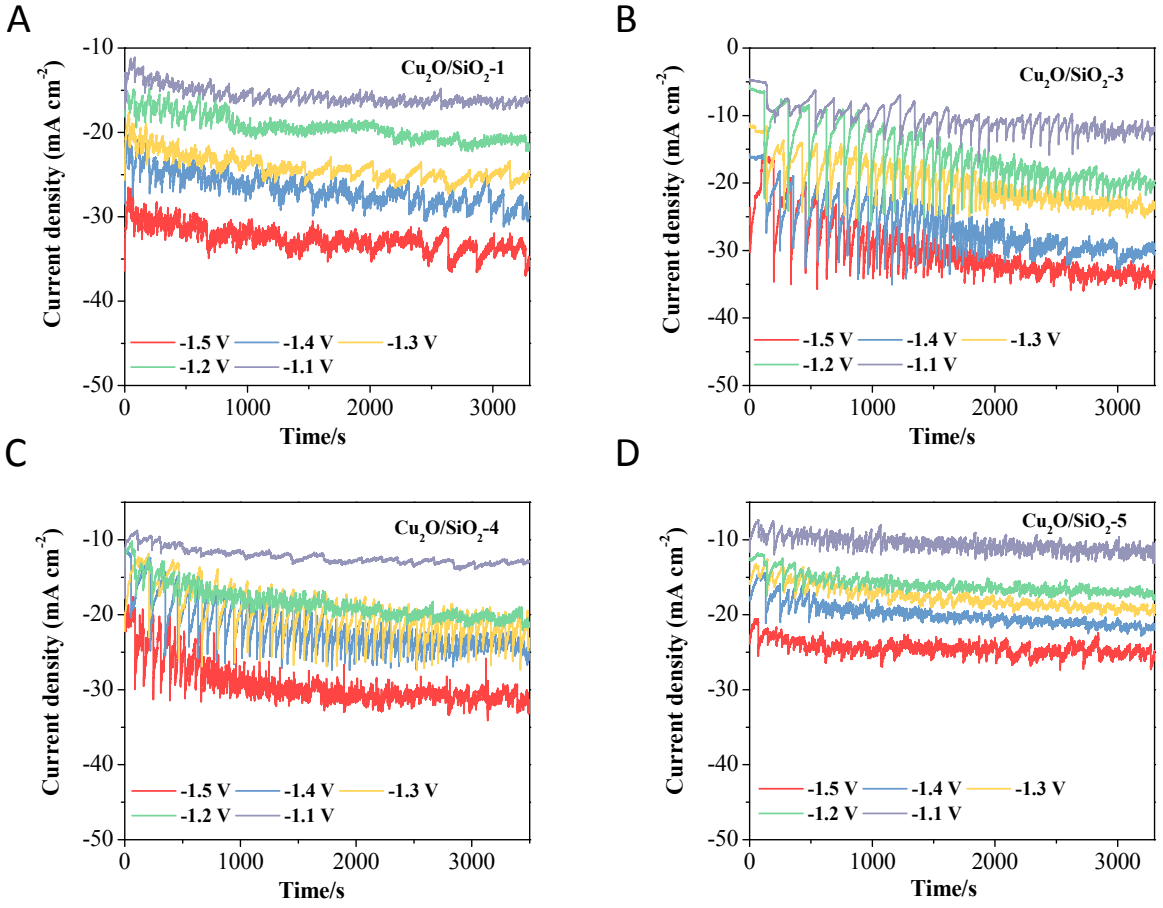

Figure S19. The i-t curves were record on (A) Cu_2O/SiO_2-1, (B) Cu_2O/SiO_2-3, (C) Cu_2O/SiO_2-4 and (D) Cu_2O/SiO_2-5 in CO_2-saturated 0.1M $KHCO_3$.

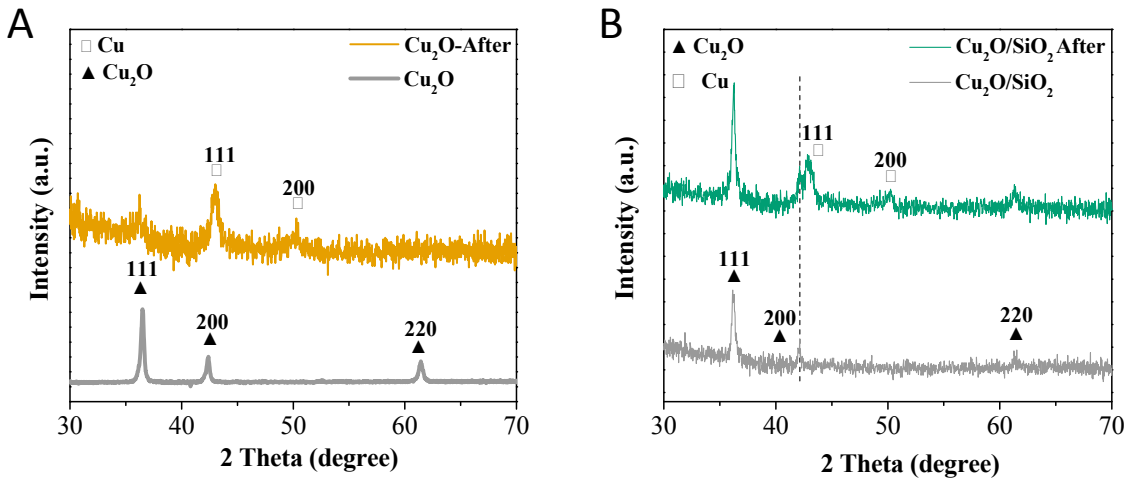

Figure S20. Crystal phase evolution analysis on (A) Cu_2O and (B) Cu_2O/SiO_2. The tests were performed on −1.2 V vs. RHE in CO_2-saturated 0.1 M $KHCO_3$.

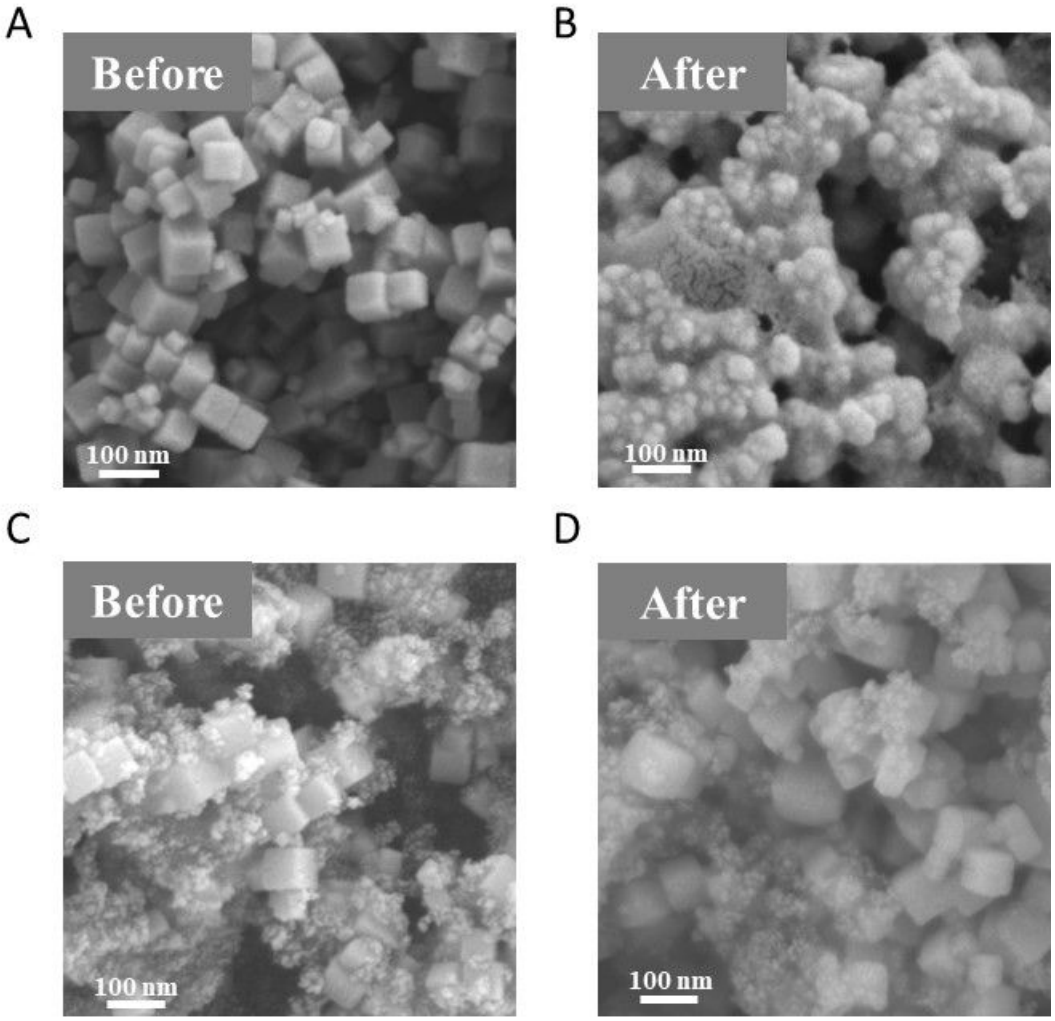

Figure S21. SEM images for Cu_2O (A, B) and Cu_2O/SiO_2 (C, D) before/after electrolysis operated at −1.2 V vs. RHE in CO_2-saturated 0.1 M $KHCO_3$.

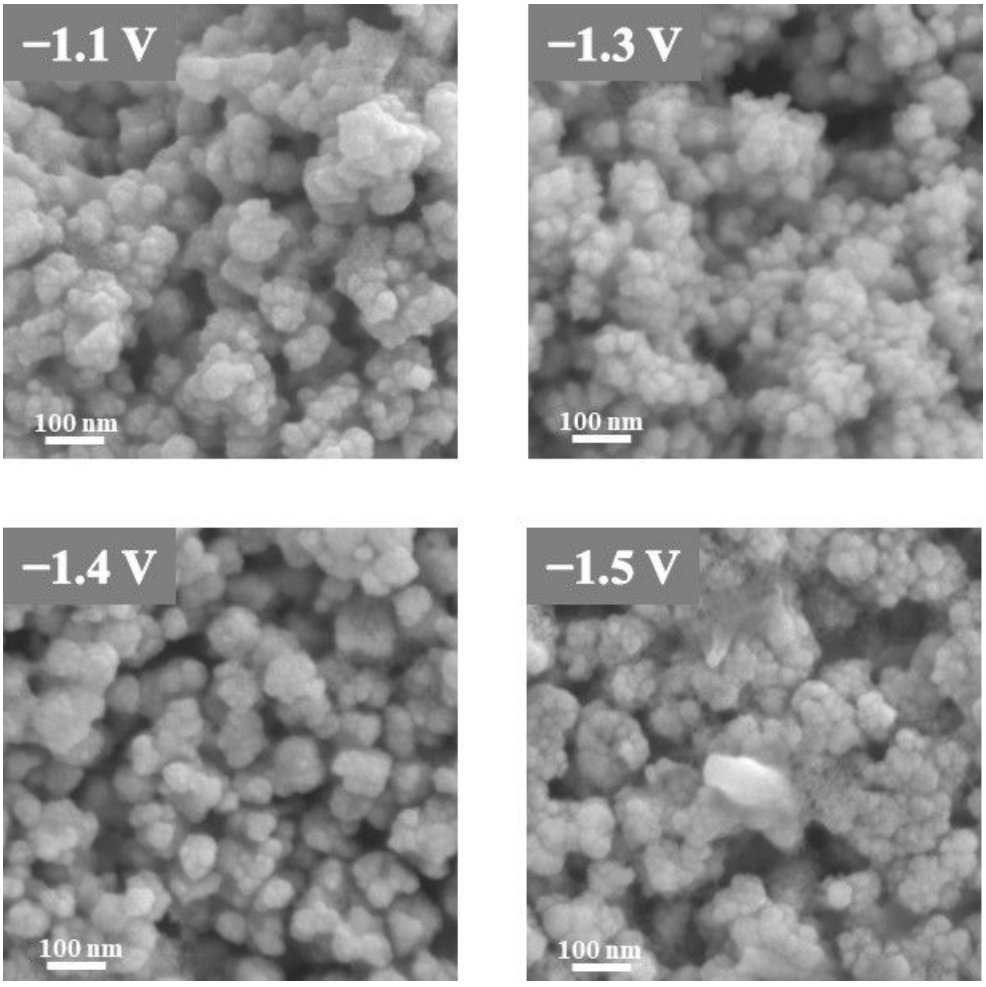

Figure S22. SEM images on the Cu_2O after electrolysis operated at various potentials in CO_2-saturated 0.1 M $KHCO_3$.

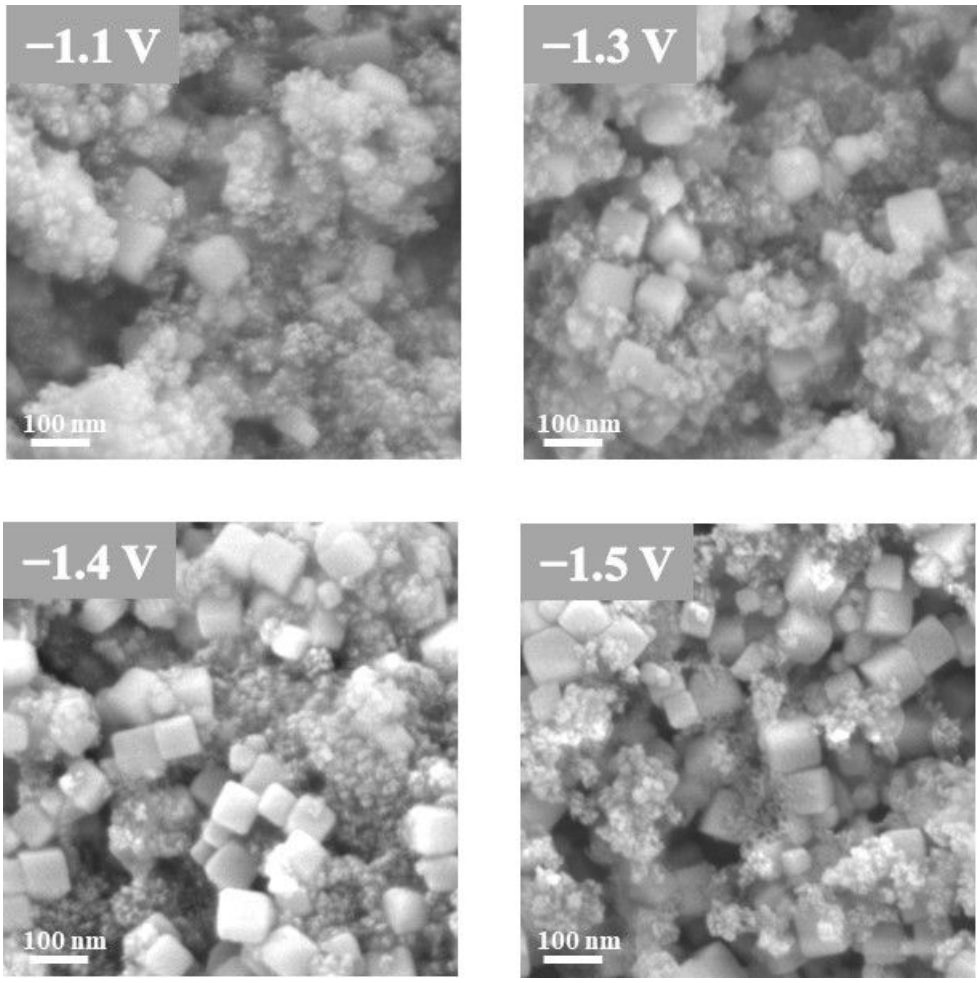

Figure S23. SEM images on the Cu_2O/SiO_2 after electrolysis operated at various potentials in CO_2-saturated 0.1 M $KHCO_3$.

Table S3. Mass fraction of Cu and Si of Cu_2O/SiO_2-1/2/3/4/5 composites using FESEM−EDS elemental analysis before and after reaction at −1.2 V in CO_2-saturated 0.1 M $KHCO_3$.

Catalysts	Before reaction			After reaction		
	Cu (wt %)	Si (wt %)	Mass Ratio (Cu/Si)	Cu (wt %)	Si (wt %)	Mass Ratio (Cu/Si)
Cu_2O/SiO_2-1	80.74	5.07	15.93	88.10	4.20	20.98
Cu_2O/SiO_2-2	71.59	9.90	7.23	78.80	7.10	11.10
Cu_2O/SiO_2-3	72.37	10.30	7.02	76.90	7.30	10.53
Cu_2O/SiO_2-4	63.80	13.90	4.59	66.90	11.30	5.92
Cu_2O/SiO_2-5	59.30	16.40	3.62	64.00	14.20	4.51

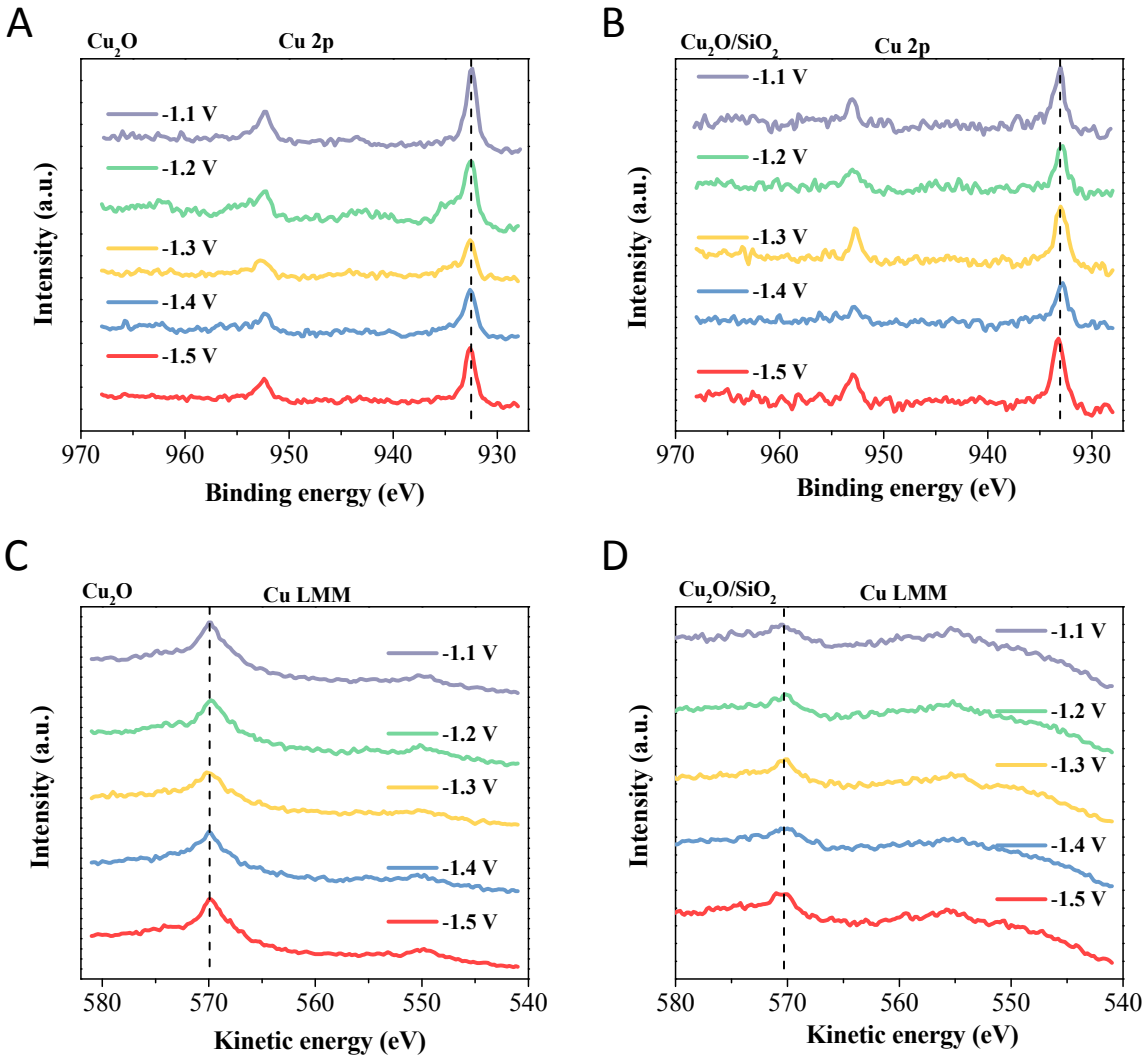

Figure S24. Cu 2p spectra (A, B) and Cu Auger LMM spectra (C, D) for Cu_2O and Cu_2O/SiO_2 after electrolysis at various potentials in CO_2-saturated 0.1 M $KHCO_3$ for specified periods.

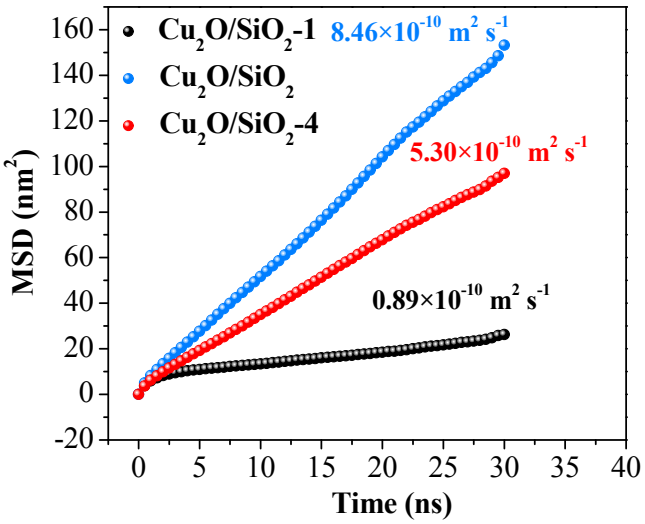

Figure S25. The dependence of mean square displacement (MSD) versus time for Cu_2O/SiO_2-1, Cu_2O/SiO_2 and Cu_2O/SiO_2-4.

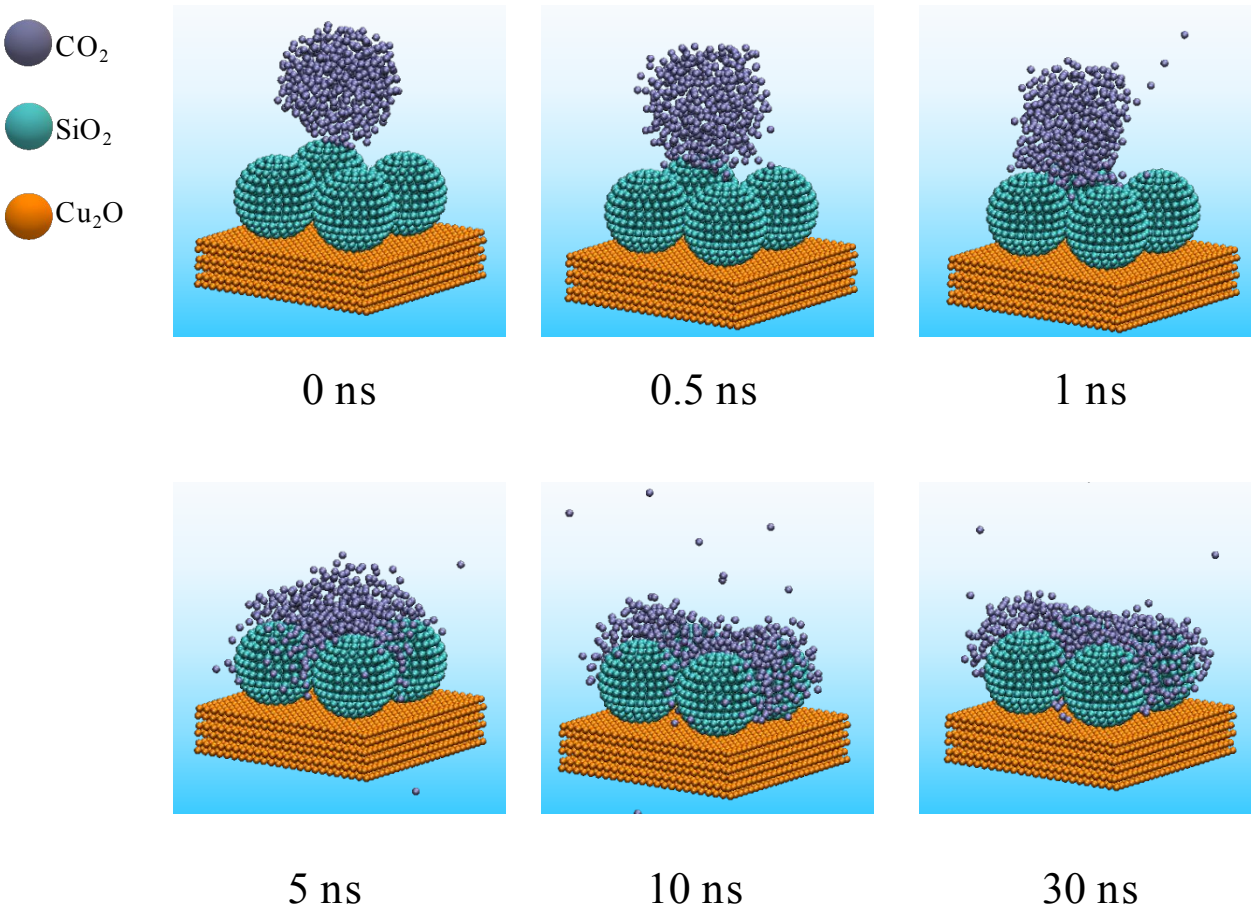

Figure S26. Evolution of typical snapshots of CO_2 diffusion dynamics on Cu_2O/SiO_2-4.

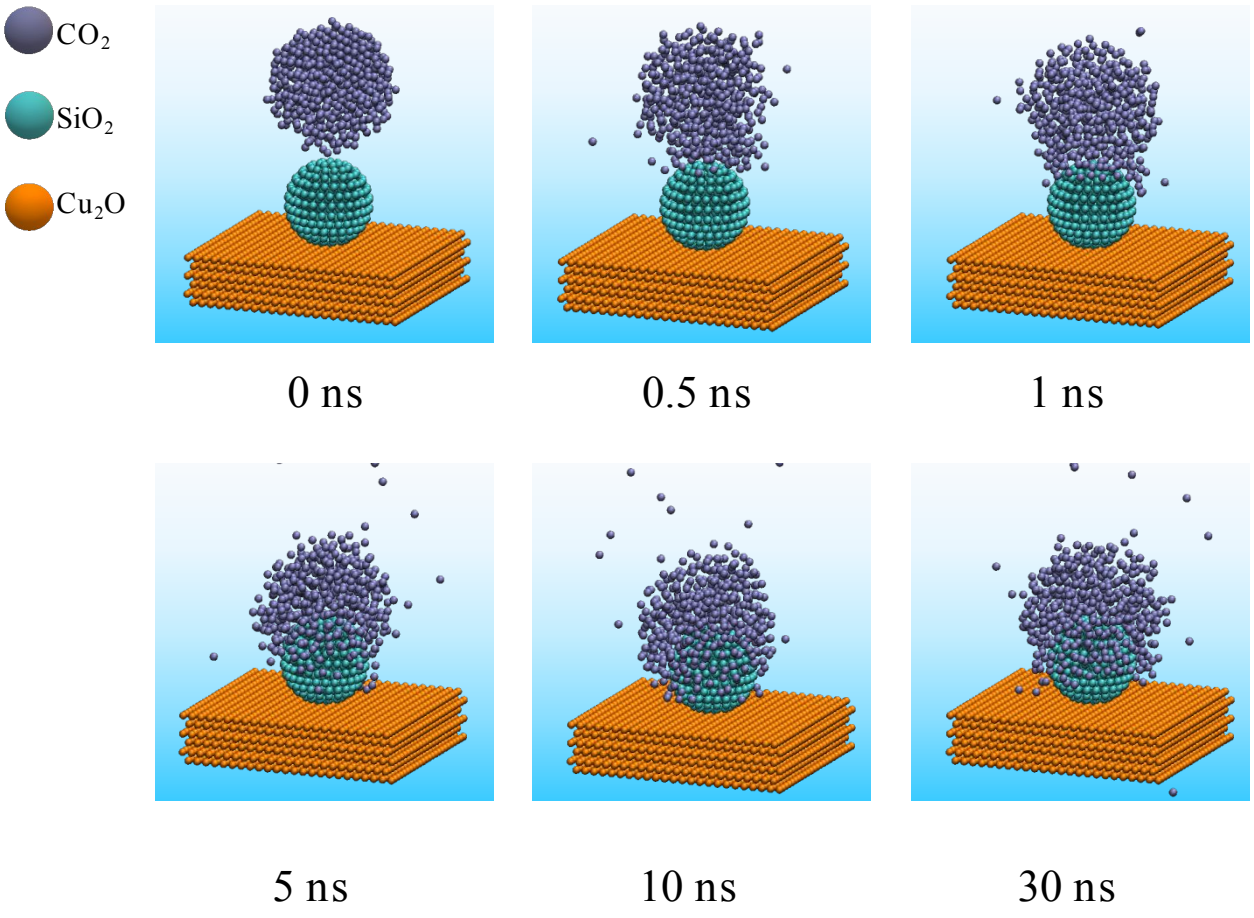

Figure S27. Evolution of typical snapshots of CO_2 diffusion dynamics on Cu_2O/SiO_2-1.

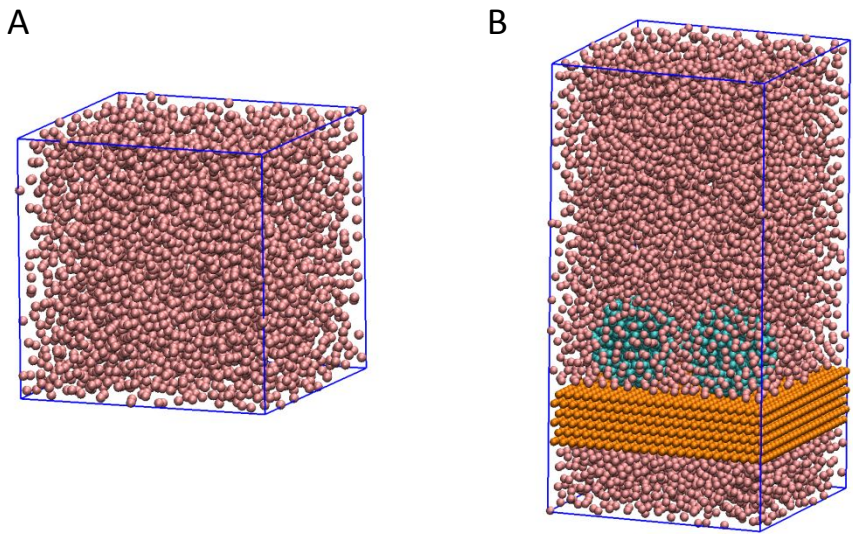

Figure S28. Water simulation box in the (A) absence and (B) presence of hydrophobic SiO_2 aerosol. H_2O molecular (pink), SiO_2 particles (cyan), and Cu_2O (orange).

References

1. Hess B.; Kutzner C.; Spoel van der D.; Lindahl E., GROMACS 4: Algorithms for Highly Efficient, Load-Balanced, and Scalable Molecular Simulation. *J. Chem. Theory Comput.* **2008,** *4,* 435-447.

2. Bai, C.; Herzfeld, J., Surface Propensities of the Self-Ions of Water. *ACS Cent. Sci.* **2016,** *2,* 225-231.

3. Kresse G.; Furthmüller J., Efficient iterative schemes for ab initio total-energy calculations using a plane-wave basis set. *Phys. Rev. B* **1996**, *54,* 11169-11186.

4. Blochl, P. E., Projector augmented-wave method. *Phys. Rev. B Condens. Matter.* **1994,** *50,* 17953-17979.

5. Perdew J. P.; Burke K.; Ernzerhof M., Generalized Gradient Approximation Made Simple. *Phys. Rev. Lett.* **1996**, *77,* 3865-3868.

6. Moller, T.; Scholten, F.; Thanh, T. N.; Sinev, I.; Timoshenko, J.; Wang, X.; Jovanov, Z.; Gliech, M.; Roldan Cuenya, B.; Varela, A. S.; Strasser, P., Electrocatalytic CO_2 Reduction on CuO_x Nanocubes: Tracking the Evolution of Chemical State, Geometric Structure, and Catalytic Selectivity using Operando Spectroscopy. *Angew. Chem. Int. Ed.* **2020**, *59,* 17974-17983.

7. Wei, Y.; Liu, J.; Cheng, F.; Chen, J., Mn-doped atomic SnO_2 layers for highly efficient CO_2 electrochemical reduction. *J. Mater. Chem. A* **2019,** *7,* 19651-19656.

8. Zhu, Z.; Li, Z.; Wang, J.; Li, R.; Chen, H.; Li, Y.; Chen, J. S.; Wu, R.; Wei, Z., Improving NiN_X and pyridinic N active sites with space-confined pyrolysis for effective CO_2 electroreduction. *eScience* **2022,** *2,* 445-452.

9. Chen, R.; Su, H. Y.; Liu, D.; Huang, R.; Meng, X.; Cui, X.; Tian, Z. Q.; Zhang, D. H.; Deng, D., Highly Selective Production of Ethylene by the Electroreduction of Carbon Monoxide. *Angew. Chem. Int. Ed.* **2020,** *59,* 154-160.

10. Wang, K.; Liu, D.; Liu, L.; Liu, J.; Hu, X.; Li, P.; Li, M.; Vasenko, A. S.; Xiao, C.; Ding, S., Tuning the local electronic structure of oxygen vacancies over copper-doped zinc oxide for efficient CO_2 electroreduction. *eScience* **2022,** *2,* 518-528.

11. Zhan, C.; Dattila, F.; Rettenmaier, C.; Bergmann, A.; Kühl, S.; García-Muelas, R.; López, N.; Cuenya, B. R., Revealing the CO Coverage-Driven C–C Coupling Mechanism for Electrochemical CO_2 Reduction on Cu_2O Nanocubes via Operando Raman Spectroscopy. *ACS Catal.* **2021**, *11,* 7694-7701.

12. Kim, J. Y.; Park, W.; Choi, C.; Kim, G.; Cho, K. M.; Lim, J.; Kim, S. J.; Al-Saggaf, A.; Gereige, I.; Lee, H.; Jung, W.-B.; Jung, Y.; Jung, H.-T., High Facets on Nanowrinkled Cu via Chemical Vapor Deposition Graphene Growth for Efficient CO_2 Reduction into Ethanol. *ACS Catal.* 2021, *11,* 5658-5665.

13. Arán-Ais, R. M.; Scholten, F.; Kunze, S.; Rizo, R.; Roldan Cuenya, B., The role of in situ generated morphological motifs and Cu(i) species in C_{2+} product selectivity during CO_2 pulsed electroreduction. *Nat. Energy* 2020, *5,* 317-325.

14. Jung, H.; Lee, S. Y.; Lee, C. W.; Cho, M. K.; Won, D. H.; Kim, C.; Oh, H. S.; Min, B. K.; Hwang, Y. J., Electrochemical Fragmentation of Cu_2O Nanoparticles Enhancing Selective C-C Coupling from CO_2 Reduction Reaction. *J. Am. Chem. Soc.* 2019, *141,* 4624-4633.

15. Han, Z.; Kortlever, R.; Chen, H. Y.; Peters, J. C.; Agapie, T., CO_2 Reduction Selective for $C_{\geq 2}$ Products on Polycrystalline Copper with N-Substituted Pyridinium Additives. *ACS Cent. Sci.* 2017, *3,* 853-859.

16. Gao, D.; Zegkinoglou, I.; Divins, N. J.; Scholten, F.; Sinev, I.; Grosse, P.; Roldan Cuenya, B., Plasma-Activated Copper Nanocube Catalysts for Efficient Carbon Dioxide Electroreduction to Hydrocarbons and Alcohols. *ACS Nano* 2017, *11,* 4825-4831.

17. Ren, D.; Ang, B. S.-H.; Yeo, B. S., Tuning the Selectivity of Carbon Dioxide Electroreduction toward Ethanol on Oxide-Derived Cu_xZn Catalysts. *ACS Catal.* **2016,** *6,* 8239-8247.

18. Hoang T., Verma S. , Ma S. , Fister T. , Timoshenko J. , Frenkel A., Kenis P., Gewirth A., Nanoporous Copper–Silver Alloys by Additive-Controlled Electrodeposition for the Selective Electroreduction of CO_2 to Ethylene and Ethanol. *J. Am. Chem. Soc.* **2018,** *140,* 5791-5797.

19. Li, H.; Liu, T.; Wei, P.; Lin, L.; Gao, D.; Wang, G.; Bao, X., High-Rate CO_2 Electroreduction to C_{2+} Products over a Copper-Copper Iodide Catalyst. *Angew. Chem. Int. Ed.* **2021,** *60,* 14329-14333.

20. Yan, X.; Chen, C.; Wu, Y.; Liu, S.; Chen, Y.-Z.; Feng, R.; Zhang, J.; Han, B., Efficient Electroreduction of CO_2 to C_{2+} Products on CeO_2 modified CuO. *Chem. Sci.* **2021**, *12,* 6638-6645.

21. Niu, Z. Z.; Gao, F. Y.; Zhang, X. L.; Yang, P. P.; Liu, R.; Chi, L. P.; Wu, Z. Z.; Qin, S.; Yu, X.; Gao, M. R., Hierarchical Copper with Inherent Hydrophobicity Mitigates Electrode Flooding for High-Rate CO_2 Electroreduction to Multicarbon Products. *J. Am. Chem. Soc.* **2021**, *143,* 8011-8021.

22. Ma, S.; Sadakiyo, M.; Luo, R.; Heima, M.; Yamauchi, M.; Kenis, P. J. A., One-step electrosynthesis of ethylene and ethanol from CO_2 in an alkaline electrolyzer. *J. Power Sources* **2016,** *301,* 219-228.